

UC San Diego

UC San Diego Previously Published Works

Title

The Role of Dielectric Screening in Organic Shortwave Infrared Photodiodes for Spectroscopic Image Sensing

Permalink

<https://escholarship.org/uc/item/79s3536j>

Journal

Advanced Functional Materials, 28(50)

ISSN

1616-301X

Authors

Wu, Zhenghui
Zhai, Yichen
Yao, Weichuan
et al.

Publication Date

2018-12-01

DOI

10.1002/adfm.201805738

Peer reviewed

The Role of Dielectric Screening in Organic Shortwave Infrared Photodiodes for Spectroscopic Image Sensing

Zhenghui Wu, Yichen Zhai, Weichuan Yao, Naresh Eedugurala, Song Zhang, Lifeng Huang, Xiaodan Gu, Jason D. Azoulay, and Tse Nga Ng*

This work examines an additive approach that increases dielectric screening to overcome performance challenges in organic shortwave infrared (SWIR) photodiodes. The role of the high-permittivity additive, camphoric anhydride, in the exciton dissociation and charge collection processes is revealed through measurements of transient photoconductivity and electrochemical impedance. Dielectric screening reduces the exciton binding energy to increase exciton dissociation efficiency and lowers trap-assisted recombination loss, in the absence of any morphological changes for two polymer variants. In the best devices, the peak internal quantum efficiency at 1100 nm is increased up to 66%, and the photoresponse extends to 1400 nm. The SWIR photodiodes are integrated into a 4 × 4 pixel imager to demonstrate tissue differentiation and estimate the fat-to-muscle ratio through noninvasive spectroscopic analysis.

1. Introduction

Photodetection in the shortwave infrared (SWIR, wavelength $\lambda = 1\text{--}3\ \mu\text{m}$) forms the foundation for many spectroscopic systems and medical applications.^[1–3] For the next generation of SWIR detectors, solution-processed semiconductors^[4–8] offer the potential to achieve scalable integrated arrays while significantly lowering processing costs. Recent progress in tuning the properties of solution-processed polymers^[8–12] has extended the spectral response of organic bulk heterojunction (BHJ) photodiodes out to 2 μm . However, the device external quantum efficiency (EQE) remains low when operating without photoconductive gain, with EQE $\leq 15\%$ in state-of-the-art organic SWIR photodiodes.^[10–13] As the BHJ/polymer bandgap is reduced, it is increasingly difficult for charge transfer (CT) excitons to dissociate due to the low internal electric field,^[14] and there is a higher rate of recombination^[15,16] impeding charge

transport and collection. To address these critical challenges, this paper demonstrates a general additive approach that enhances dielectric screening and can double the device EQE in two different SWIR BHJs. Through measurements of transient photocurrent and electrochemical impedance, we delineate the effect of high dielectric constant on exciton dissociation and charge collection processes, to pinpoint the key mechanisms essential to raise detectivity in organic SWIR devices.


The role of high dielectric constant materials in organic photodiodes remains under debate.^[17–19] The dielectric constant or permittivity ϵ_r represents the polarizability of a material. Increasing polarizability^[19] offers a path to screen Coulombic

interactions between electron–hole pairs and stabilize free carriers, thus dielectric screening may be particularly important for SWIR devices which suffer from poor exciton dissociation. Prior studies^[20–22] have shown a reduction in exciton binding energy with higher ϵ_r in BHJ solar cells. On the other hand, there are mixed results^[18,19] where high- ϵ_r materials did not improve the device performance. It is unclear why some BHJ systems only marginally benefit from tuning ϵ_r while others are greatly enhanced. Thus, this work clarifies conditions when increasing ϵ_r would be useful, in the context of two photoreponsive SWIR donor polymers incorporated into BHJs. The BHJ permittivity is increased by adding camphoric anhydride, which is an insulating molecule with one of the highest permittivities among organic solids (ϵ_r is up to 24).^[21,23] The high- ϵ_r additive leads to different mechanisms of efficiency improvement in the polymer variants. These results provide insight into the relationship between dielectric properties and device performance. By tuning ϵ_r we exceed the state-of-the-art, achieving a peak EQE = 26% at $\lambda = 1100\text{ nm}$ and zero bias in organic photodiodes, with the peak detectivity comparable to commercial germanium photodiodes.

As the detectivity of our SWIR devices approaches the level of conventional germanium photodiodes, the organic photodiodes become practical for system integration. For a feasibility demonstration, the photodiodes are integrated with switching diodes into an active matrix 4 × 4 pixel array. The array enables imaging of sample structures and interrogation of the composition through spectral analysis. For example, when imaging in the range of $\lambda = 1150\text{--}1250\text{ nm}$, the array shows the capability to map the percentage of fat tissues underneath muscles, which

Dr. Z. Wu, Y. Zhai, W. Yao, Prof. T. N. Ng
Department of Electrical and Computer Engineering
University of California San Diego
9500 Gilman Drive, La Jolla, CA 92093-0407, USA
E-mail: tnn046@ucsd.edu

Dr. N. Eedugurala, S. Zhang, L. Huang, Prof. X. Gu, Prof. J. D. Azoulay
School of Polymer Science and Engineering
University of Southern Mississippi
118 College Drive #5050, Hattiesburg, MS 39406, USA

 The ORCID identification number(s) for the author(s) of this article can be found under <https://doi.org/10.1002/adfm.201805738>.

DOI: 10.1002/adfm.201805738

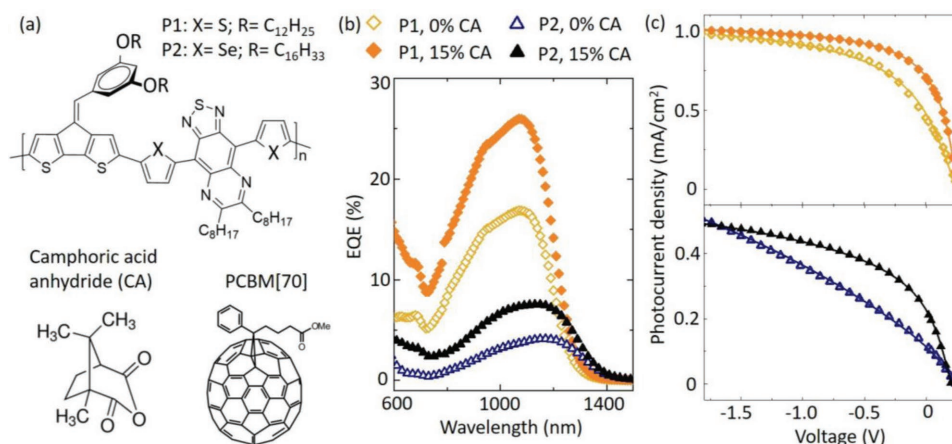


Figure 1. a) Chemical structures of the bulk heterojunction materials. b) External quantum efficiency of the photodiodes at zero applied voltage versus incident wavelength. c) Photocurrent density versus applied voltage under incident light with $\lambda = 1100$ nm and an intensity of 3.2 mW cm^{-2} . The data are fitted to Equation (3) as depicted by the solid lines.

is applicable for atherosclerosis diagnosis and other biomedical spectroscopic imaging applications.

2. Results and Discussions

The BHJ blends are comprised of a polymeric donor and a fullerene-derivative acceptor in 1:2 weight ratio, with either 0 or 15% by weight of the high- ϵ_r additive camphoric anhydride (CA). The chemical structures of the materials are shown in Figure 1a. The two SWIR polymers differ by the thiophene or selenophene spacer and side-chain lengths, and the P2 polymer shows a slightly narrower bandgap than P1. The device structure, energy levels of the materials, and dark current–voltage characteristics are shown in Figure S1 (Supporting Information). For the BHJs in this work, the optimal percentage of CA is around 15%, and the CA additive raises the permittivity ϵ_r as listed in Table 1 (with supporting measurements in Figure S2, Supporting Information). The device current within the displayed voltage range was stable and did not show hysteresis. This paper will focus on the four BHJ compositions in Figure 1b to study the influence of CA on the photocurrent generation steps, namely, (i) the exciton dissociation process followed by (ii) charge transport and collection.

Before delving into efficiencies of individual steps, we note that the overall EQE is up to two times higher in devices with

15% CA than without the additive. In Figure 1c, the electric-field dependence is reduced in photocurrent of devices with CA. The photodiode with P1 and CA shows a peak EQE of 26% at 0 V bias and 35% at -1 V for $\lambda = 1100$ nm. To the best of our knowledge, this EQE is the highest achieved for SWIR organic devices without resorting to photoconductive gain which limits the bandwidth.

2.1. Study of Film Morphologies

Since the origin for performance improvements in devices with CA may be due to changes in morphology, the BHJs were measured by grazing-incidence X-ray diffraction (GIXD) and resonant soft X-ray scattering (R-SoXS) to study film nano- and microstructures. Both measurements show there is no discernible morphological change from adding CA at 15% weight ratio, with respect to the crystalline domain for donor polymers and the phase separation scale between the donor and the acceptor. In Figure 2a, all four BHJ thin films show broad diffraction peaks at $q = 1.26 \text{ \AA}^{-1}$ which can be attributed to the scattering from amorphous PC₇₁BM and disordered polymer regions. The structures of the P1 and P2 BHJ samples are different on the nanometer scale; for instance, in Figure 2b, broad shoulders in the scattering profile are observed around $q = 0.02 \text{ \AA}^{-1}$ for the P1 BHJ and at 0.01 \AA^{-1} for the P2 BHJ. These shoulders indicate the domain size of donor/acceptor phase segregation, which is 30 nm for films with P1 and 60 nm with P2. Nonetheless, the phase segregation is the same between films with or without CA. Thus, we rule out morphological changes in our films with CA and concentrate on understanding the effects of CA on electronic properties in the following sections. These measurements do however point to additional gains in performance upon further optimization of the morphology.

Table 1. Device parameters for photodiodes with different bulk heterojunction compositions. The values for $\eta_{\text{dissociate}}$, η_{collect} , EQE, and IQE are obtained with incident light $\lambda = 1100$ nm and at an applied bias of 0 V. The effective carrier lifetimes (τ_r) are measured in the dark at an applied bias of 0 V.

	Measured values				Obtained by fitting to Equation (3)		
	ϵ_r	EQE [%]	$\langle \mu \rangle$ ($10^{-4} \text{ cm}^2 \text{ V}^{-1} \text{ s}^{-1}$)	τ_r [ms]	$\eta_{\text{dissociate}}$ [%]	η_{collect} [%]	IQE [%]
P1, 0% CA	3.5	17	3.4	1.48	≈ 100	43 ± 4	43 ± 4
P1, 15% CA	4.7	26	6.5	1.83	≈ 100	66 ± 6	66 ± 6
P2, 0% CA	3.1	3.8	4.8	0.24	15 ± 3	55 ± 9	8 ± 3
P2, 15% CA	4.6	7.8	9.8	0.46	50 ± 13	55 ± 6	27 ± 6

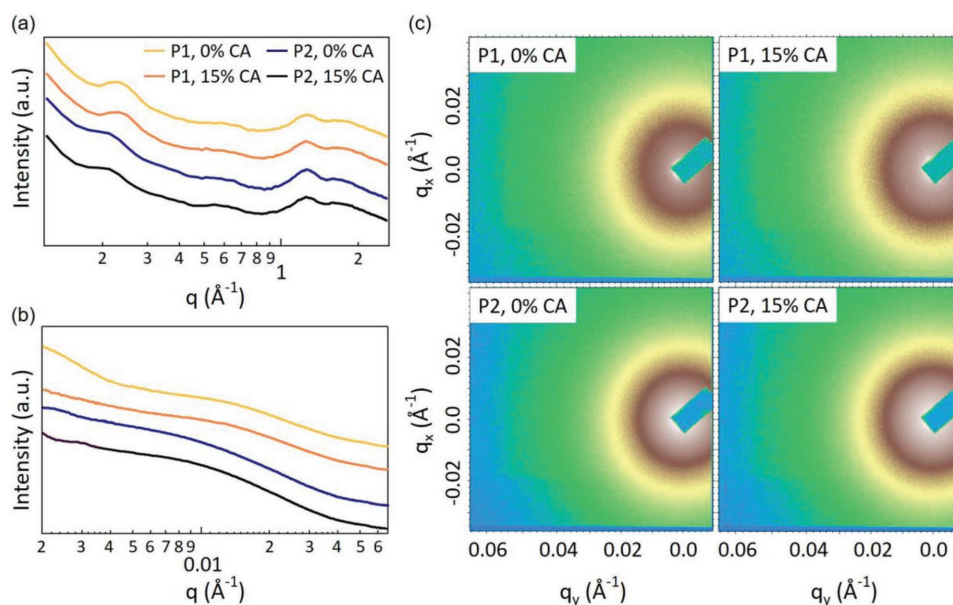


Figure 2. Line profiles of the scattering intensity versus scattering vector in a) GIXD and b) R-SoXS of bulk heterojunction films. c) 2D R-SoXS patterns of BHJ films with different donor polymers and percentages of CA.

2.2. Effect of Increasing ϵ_r on Photocurrent Generation Steps

Measuring transient photocurrent^[14,24,25] allows us to probe the CT exciton dissociation efficiency and the kinetics of charge transport and recombination. By using nanosecond laser pulses to photogenerate charge carriers, the transient photoconductivity (TPC) in **Figure 3** is shown to originate from the mobile carriers at short times before significant bimolecular recombination or charge collection occurs. We first compare the initial carrier densities to see if adding CA would increase CT exciton dissociation and minimize nonradiative recombination. Nonradiative recombination is a loss mechanism by thermal decay, in which the energy is lost to electron–phonon coupling. Next,

the carrier transit time and recombination time are extracted to understand how charge transport is affected by CA increasing ϵ_r in SWIR photodiodes. The EQE is a product of the efficiencies of photon absorption, exciton dissociation, and charge collection: $\text{EQE} = \eta_{\text{absorb}} \eta_{\text{dissociate}} \eta_{\text{collect}}$. We will quantify the efficiency of each photocurrent generation step by fitting to current density–voltage characteristics, which provide independent checks on the TPC results.

2.2.1. Examination of Charge-Transfer Exciton Dissociation Efficiency

The initial carrier density $N(V, t_{0+})$ is proportional to the transient photocurrent density,^[24] expressed as $J_{\text{ph}}(V, t_{0+}) = q(\mu)N(V, t_{0+})$

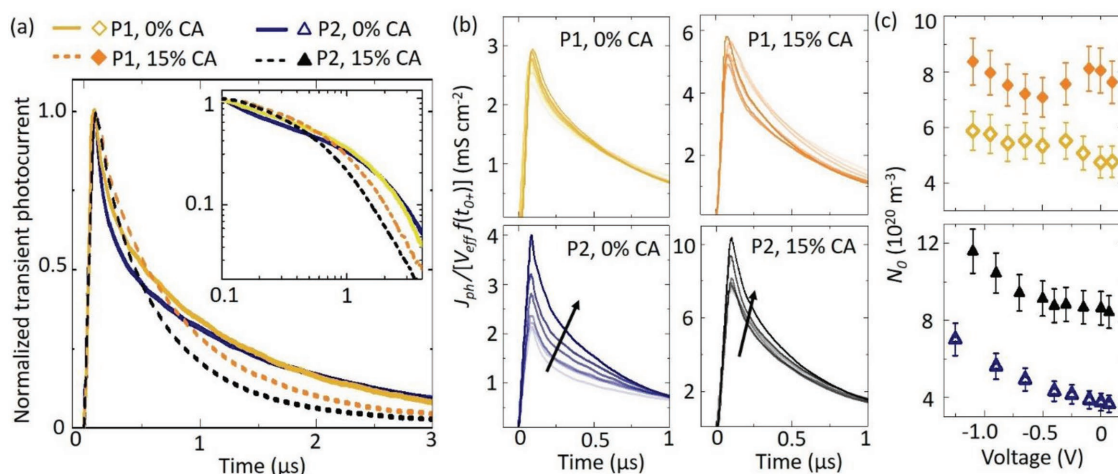


Figure 3. a) Normalized transient photocurrent versus time, as a bias of 0.1 V was applied to the photodiodes. The inset shows the same data in logarithmic scale. b) Adjusted photoconductivity density versus time. The applied bias was varied from 0.1 to -1.5 V as indicated by the arrow direction. c) Initial carrier concentration versus applied voltage. The error bars originated from the uncertainties in the transit time τ_{transit} , which is the intersection point where the TPC signal switches its slope^[26] as shown in the inset of (a).

V_{eff}/d , where t_{0+} denotes the time just after the illumination pulse, q is the elementary charge, $\langle\mu\rangle$ is the average mobility, d is the BHJ layer thickness, and $V_{\text{eff}} = V_{\text{bi}} - V$ is the effective voltage from subtracting the applied voltage V from the built-in voltage V_{bi} . However, due to a RC delay τ_{RC} in the measurement circuit, the TPC signals rise to peak photocurrent only at τ_{RC} . The ratio between values at τ_{RC} and at t_{0+} is estimated to be a factor of $f(t_{0+}) = (1 - \tau_{\text{RC}}/\tau_{\text{transit}})^2$ as explained in detail in Figure S4 (Supporting Information). The transit time τ_{transit} is the intersection point where the TPC signal switches its slope^[26] as shown in the inset of Figure 3a. Taking this factor of $f(t_{0+})$ into account, the adjusted TPC densities are displayed in Figure 3b, from which the peak values are converted into initial carrier densities in Figure 3c

$$N_0(V) = J_{\text{ph}}(V, \tau_{\text{RC}}) d / q \langle\mu\rangle V_{\text{eff}} f(t_{0+}) \quad (1)$$

All the parameters used in the $N_0(V)$ calculations are directly measured quantities or material constants.

In P1 BHJs, applying a bias voltage did not affect the initial carrier densities which remain constant regardless of a change in the external bias or material ϵ_r . There was 30% difference in the initial carrier densities between the P1 devices with or without CA. However, this difference was small and might be affected by incident light intensity and BHJ thickness difference. While cross-sample comparisons might be affected by optical effects, the $N_0(V)$ trends within individual samples were highly reproducible. The constant $N_0(V)$ for P1 BHJs indicates a maximally efficient exciton dissociation process, that all the electron–hole pairs are already separated into free carriers without the need of an external electric field.

On the other hand, in P2 BHJs the $N_0(V)$ increases as the bias voltage is varied from 0.1 to -1.5 V, and the addition of CA further doubles the initial carrier densities. The dissociation efficiency in P2 BHJs is not topped out and needs improvements. The applied voltage provides an additional electric field to assist in exciton separation in P2 BHJs, and hence initial charge densities become higher with an increasing reverse bias. Alternatively, adding CA to the P2 BHJ significantly increases initial carrier densities, therefore indicating better CT exciton dissociation efficiency over the whole voltage range.

The incorporation of CA in BHJs leads to higher ϵ_r (measured values in Table 1), which in turn lowers the exciton binding energy. The exciton binding energy is $E_{\text{B}} = q^2 / (4\pi\epsilon_0\epsilon_r a)$, dependent on the internal electron–hole pair delocalization distance a and the surrounding permittivity ϵ_r , while ϵ_0 is the permittivity of vacuum. Higher permittivity indicates a greater ability to screen and stabilize charge and reduce the energy cost for an exciton to dissociate into free carriers. There is reduced field dependence in the P2 device after adding CA. In Figure 3c, for the P2 device without CA, the initial carrier density N_0 increased from $4 \times 10^{20} \text{ m}^{-3}$ to $7 \times 10^{20} \text{ m}^{-3}$, which is a 75% change in N_0 due to the applied electric field. For the P2 device with CA, N_0 increased by only 22% from 9×10^{20} to $11 \times 10^{20} \text{ m}^{-3}$ under the same electric field.

Figures 3c and 1c show consistent results that the P2 devices were limited by field-dependent generation of carriers: the P2 photocurrent–voltage curves did not plateau in Figure 1c, whereas the P1 devices reached saturation with reverse bias.

Figure 3 indicates that the addition of CA influences the CT exciton dissociation process greatly in P2 but not in P1 blends, since P1 BHJs are not limited by dissociation in the first place.

2.2.2. Examination of Charge Collection Efficiency

Although adding CA does not change η_{absorb} and $\eta_{\text{dissociate}}$ in P1 devices, it does lead to an increase in EQE in Figure 1b and must be due to more effective charge collection. Thus, we analyze the improved η_{collect} by examining transport parameters and the density of states (DOS). The transport parameters, including the average mobility $\langle\mu\rangle$ and the effective carrier recombination lifetime τ_r , are measured to be higher in both P1 and P2 BHJs with CA as listed in Table 1. The average mobility is determined from the TPC transit time using the relationship $\langle\mu\rangle = d^2 / (V_{\text{eff}} \tau_{\text{transit}})$. In the inset of Figure 3a, the transit time τ_{transit} is the intersection point where the TPC signal switches its slope^[26] and the devices with CA and higher ϵ_r show faster transit. Beyond the transit time the TPC signal is no longer dominated by collection of photogenerated carriers, and the measured current then originates from release of trapped charges at recombination centers. The current beyond $2 \mu\text{s}$ is lower in devices with CA, which suggests a lower density of traps than the ones without CA.

The recombination lifetime τ_r is estimated from electrochemical impedance spectroscopy in Figure 4. These impedance measurements are taken in the dark, in order to put an upper boundary on τ_r . The τ_r values in Table 1 would decrease under irradiation when there is a greater number of carriers increasing the likelihood of recombination. Figure 4a is known as the Nyquist plot in which the real and the imaginary components of impedance are recorded as the measurement frequency is varied. The same data are displayed as imaginary impedance $\text{Im}(Z)$ versus frequency in Figure 4b. The frequency corresponding to the peak $\text{Im}(Z)$ is the inverse of the carrier lifetime^[27] by $f_r = 1/\tau_r$. The effective carrier lifetime is extended in the BHJs with CA, because of better screening which reduces charge interaction and trap-assisted recombination.

To understand the dispersive transport in our devices, the sub-bandgap DOS distribution is inferred from the capacitance versus frequency measurements in Figure 4c. The DOS connects the materials composition and electronic properties, particularly to count localized trap states.^[25,28] In Figure 4c, only the carriers in states shallower than the trap energy E_{ω} can be released quickly enough to contribute to the capacitance at each measurement frequency ω . The trap energy is related to the measurement frequency by $E_{\omega} = kT \ln(\omega_0/\omega)$, where k is the Boltzmann constant, T is the temperature, and ω_0 is the rate prefactor for thermal excitation from the trap and assumed to be 10^{12} s^{-1} in typical organic photodiodes.^[28] Based on analysis in refs. [28,29], the trap DOS distribution is

$$\text{DOS}(E_{\omega}) = - \frac{V_{\text{bi}}}{qA k T} \frac{\partial C(\omega)}{\partial \ln(\omega)} \quad (2)$$

where $C(\omega)$ is the capacitance measured with an ac perturbation of angular frequency ω . Here, the built-in potential $V_{\text{bi}} \approx 0.25$ V (Figure 1c), and temperature is ≈ 300 K. The device area

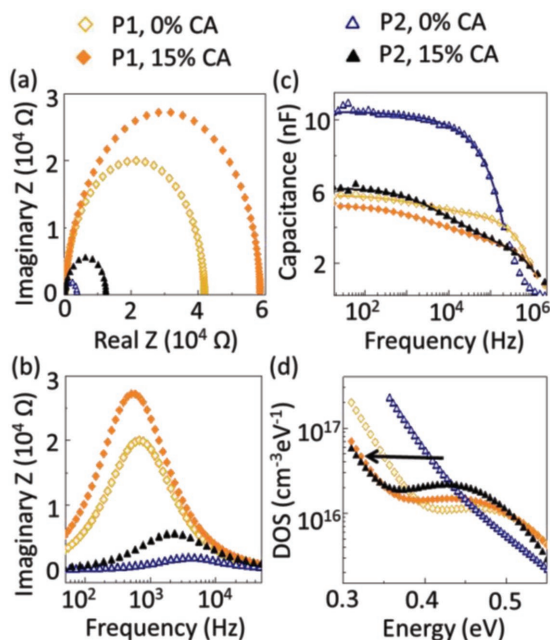


Figure 4. a) Real versus imaginary components of impedance. b) Imaginary impedance versus frequency. c) Capacitance versus frequency, in which the solid lines were best fits to Equation (S1) (Supporting Information). d) The density of states as extracted from (c) versus energy from the band edge. All the measurements are done in the dark with a dc bias at 0 V and an ac excitation of 20 mV.

is $A = 9 \text{ mm}^2$, and the BHJ thickness d is listed in Table S1 (Supporting Information). Note that the capacitance measurement cannot distinguish between electron and hole traps and reports the sum. A rapid change in slope $dC/d\ln(\omega)$ indicates an increase of the trap DOS at the corresponding energy by Equation (2).

In Figure 4c, there is one transition in slope around 0.1 MHz for the devices without CA, while the ones with CA show different characteristics with an additional transition around

1 kHz. This latter trend means there are separated groups of shallow and deep traps centered at different energy levels, as displayed in Figure 4d and further illustrated in Figure 5 and modeled in details in Table S2 (Supporting Information). The energy level of deep traps is not significantly changed and may have a small additional contribution from CA, and the built-in potential increases only slightly by <50 meV in devices with CA. However, the addition of CA into BHJs shifts the exponential bandtails to lower energy levels, which reduces the energy barrier for localized charges to hop back into the mobile transport band. Charge transport is improved because the shallow trap distributions are shifted to lower energy, and less energy is required to pull charge carriers out from trap states. Thus, charge collection rises because of a decrease in the bandtail trap density and improved carrier transport in devices with CA.

2.2.3. Comparison of Contributions to IQE by Fitting to Photocurrent–Voltage Characteristics

The effect of CA on each photocurrent generation step is quantified further by fitting to the photocurrent–voltage characteristics to determine $\eta_{\text{dissociate}}$ and η_{collect} . Based on a model in our previous work,^[14] the steady-state photocurrent density J_{phss} is a function of the effective electric field $E_{\text{eff}} = V_{\text{eff}}/d$

$$J_{\text{phss}} = J_{\text{sat}} \eta_{\text{collect}}(E_{\text{eff}}) \eta_{\text{dissociate}}(E_{\text{eff}}) \quad (3)$$

with

$$\eta_{\text{collect}}(E_{\text{eff}}) = \frac{2\mu\tau E_{\text{eff}}}{d} \left[1 - \exp\left(-\frac{d}{2\mu\tau E_{\text{eff}}}\right) \right] \quad (\text{part a}) \quad (4)$$

$$\eta_{\text{dissociate}}(E_{\text{eff}}) = \frac{4}{a^3 \sqrt{\pi}} \int_0^\infty \frac{k_D}{k_D + k_R} x^2 \exp(-x^2/a^2) dx \quad (\text{part b}) \quad (5)$$

The parameter J_{sat} is the saturation current density dependent on incident light intensity, and $J_{\text{phss}}/J_{\text{sat}} = \text{IQE}$ is the internal

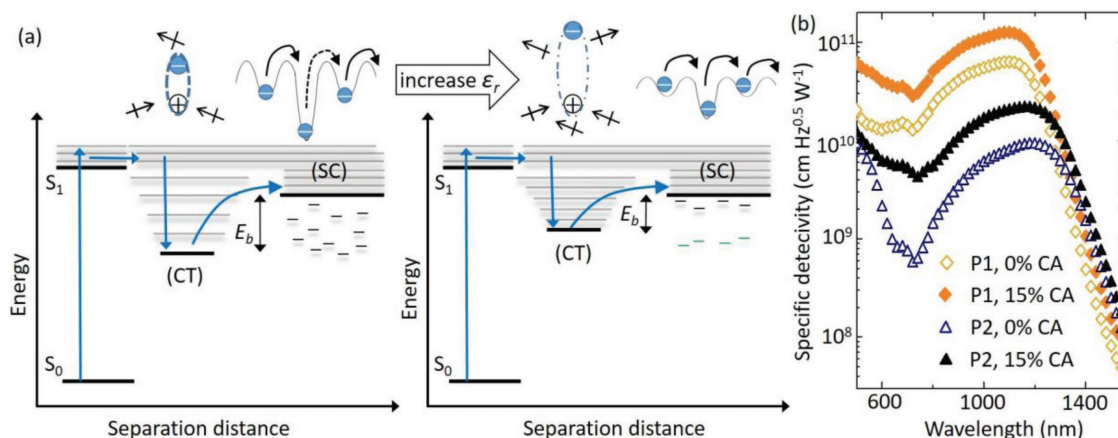


Figure 5. a) Schematic diagrams illustrating the effects of dielectric screening on charge-transfer (CT) dissociation and separated charge (SC) collection. represents a dipole. As the permittivity is increased in a bulk heterojunction, the exciton binding energy E_b is reduced. The CA additive contributes a small amount of deep traps (green), but the density of shallow bandtail states (black) is shifted to a lower energy level. Hopping transport is more efficient with lower hopping barriers and less loss from trap-assisted recombination. b) Specific detectivity at zero bias voltage versus incident light wavelength.

quantum efficiency that excludes the light absorption efficiency. For η_{collect} the fit variable $\mu\tau$ is the mobility-lifetime product that characterizes the capture cross section and density of recombination centers. The $\eta_{\text{dissociate}}$ expression^[30] is dependent on the rates of exciton dissociation k_{D} and recombination k_{R} . We assume a typical exciton delocalization length^[30] $a = 1.3$ nm. The

dissociation rate is $k_{\text{D}}(E_{\text{eff}}) = \frac{3q\langle\mu\rangle}{4\pi\epsilon_0\epsilon_r a^3} \exp(-E_{\text{B}}/kT)[1+b+\dots]$, with $b = \frac{q^3 E_{\text{eff}}}{8\pi\epsilon_0\epsilon_r (kT)^2}$. Since the parameters in k_{D} are all meas-

urable as discussed in TPC results, the variable we changed during data fitting is the recombination rate k_{R} . While the above equations look complicated, actually only two variables, $\mu\tau$ and k_{R} , are adjusted to obtain great fits to the data as shown in Figure 1c. The fit values are reported in Table S1 (Supporting Information). Moreover, the fitting process is also simplified by the prior results from TPC measurements. For example in the case of P1 BHJs, the initial carrier density is shown to be independent of electric field, indicating the dissociation efficiency is near 100%. As such, the fits to P1 devices do not require part b of Equation (3) and are reverted to a simple adjustment of a single variable $\mu\tau$ to determine η_{collect} .

The efficiency percentages are listed in Table 1. For SWIR photodiodes based on P1, incorporating CA mainly enhances the charge collection efficiency, raising η_{collect} from 43 ± 4 to $66 \pm 6\%$. For the devices based on P2, the addition of CA significantly improves $\eta_{\text{dissociate}}$ from 15 ± 3 to $50 \pm 13\%$; η_{collect} is not noticeably changed but the accuracy is limited by uncertainties in the fits. At the very least, putting CA into P2 BHJs does not degrade η_{collect} , and it is likely beneficial to the charge collection step, because TPC and DOS measurements show increased carrier lifetime and reduced bandtail states. As the $\text{EQE} = \text{IQE} \times \eta_{\text{absorb}}$, the BHJs show $\eta_{\text{absorb}} \approx 40\%$, which can be increased by light scattering or other light management optics to further optimize EQE in the future. The results here highlight the multiple mechanisms that are impacted by increasing ϵ_r in organic photodiodes. Tuning dielectric permittivity is often credited for optimizing exciton dissociation^[20–22] to reduce electronic-vibrational coupling^[31] between excited charge transfer and ground states. However as shown in this study, dielectric screening extends beyond promoting exciton dissociation and plays a role in improving charge collection. Particularly for polymers like P1 and materials for solar cells, many of which are not limited by dissociation,^[32] the benefit of dielectric screening on transport should be emphasized as it leads to an unprecedented IQE of 66% in organic SWIR photodiodes.

In comparing the device performance of P1 and P2 BHJs without CA, we see that the films of P1 and P2 systems show different extents of phase segregation that influences limiting factors to efficiency. According to R-SoXS in Figure 2, the P1 BHJ shows higher intermixing with 30 nm phase segregation compared to the P2 BHJ with 60 nm phases. This small domain size offers many interfaces to help the dissociation efficiency but constrains charge transport in P1 BHJs, and vice versa for P2 BHJs. In addition to energy level differences, these morphological properties explain why the two BHJ systems have different bottlenecks, with P1 limited by η_{collect} while P2 is low in $\eta_{\text{dissociate}}$ (Table 1).

However, the R-SoXS and GIXD diffraction patterns were the same before and after CA was added in the two systems. A small amount of CA, below 15% by weight, did not cause significant changes in morphology because of the weak molecular interaction between CA molecules and the BHJ molecules. CA is highly polar, while SWIR polymers and fullerenes are nonpolar molecules. The film morphology is undistributed probably due to the weak interaction between polar molecules and nonpolar molecules, and in disordered BHJs there is free volume space to accommodate the additives. When the percentage of CA additive is increased beyond 27%, the BHJ morphology is affected by the additive, manifested by an increase in dark current as shown in Figure S2 (Supporting Information).

The CA additive is expected to improve the performance of organic SWIR devices if the devices are limited by: (1) poor CT exciton dissociation, as manifested by strong electric-field dependence in the photocurrent–voltage characteristics; (2) poor charge collection due to recombination loss through the localized states in the bandtail. The P1 and P2 devices with 15% CA showed better stability compared to their counterparts without CA. Encapsulated P1 devices with CA retained 85% of their initial photocurrent after one month of dark storage in air, while the devices without CA retained only 60%. Encapsulated P2 devices with CA showed 70% of their initial photocurrent after 15 d of dark storage in air, while the devices without CA retained only 10%. When choosing high-permittivity additives, the additive should be able to easily blend into the BHJ without interfering with the film morphology, and the additive should show a high dielectric constant so that a small amount can increase the overall polarizability of the BHJ.^[17,19] Additives that satisfy these requirements will have similar effects as CA.

Here, we return to the question of why earlier works demonstrate a discrepancy in results employing high- ϵ_r materials. In prior work, as materials structures are changed to increase permittivity,^[18,33] there are morphological changes that may counteract the electronic effects from high permittivity. For example, CA has been used in organic solar cells,^[21] but the performance reaches a plateau when the CA forms crystals and alters BHJ phase segregation. In our materials sets, the addition of 15% CA does not noticeably affect morphology and therefore allows us to distinguish the specific electronic mechanisms that improve $\eta_{\text{dissociate}}$ and η_{collect} as summarized in Figure 5a. Moreover, prior work has focused on materials with wider bandgaps for devices which operate in the visible spectrum,^[18–22] but the CA additive is more effective in SWIR materials, for which the higher recombination probability at narrow bandgaps is a consequence of the energy gap law.^[34] Thus, increasing dielectric screening is particularly relevant for SWIR devices, and the CA additive is promising for raising ϵ_r without affecting BHJ morphologies.

Figure 5b displays the detectivity metric of our photodiodes. Detectivity is the signal-to-noise ratio and expressed as $D^* = (A\Delta f)^{0.5} R/i_n$, where $R = \text{EQE}(\lambda q/hc)$ is the responsivity, h is Planck's constant, c is the speed of light, A is the effective photodetector area, Δf is the detection bandwidth, and i_n is the noise current measured in the dark. The measured noise current in photodiodes with CA is lower than the devices without CA as seen in Figure S5 (Supporting Information), because longer carrier lifetime reduces thermal generation-recombination

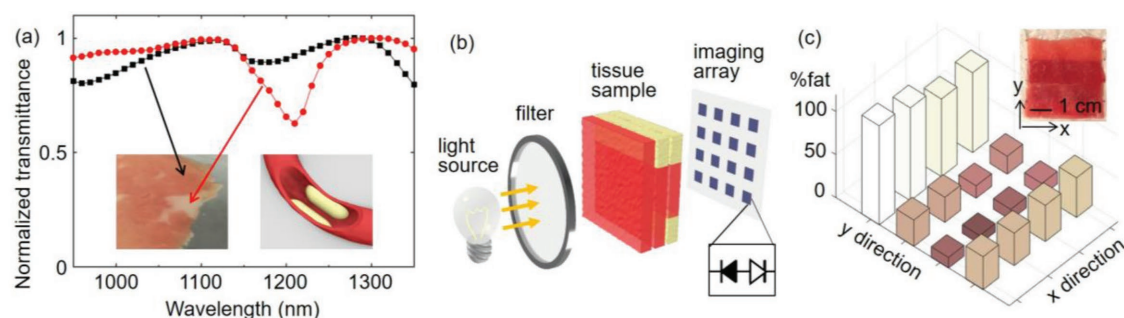


Figure 6. a) Normalized transmittance spectra of muscle (black) and fatty tissues (red). The inset schematic illustrates the scenario of fatty deposits clogging an artery. b) Measurement setup using the organic array for SWIR spectral imaging. c) Percentage of fatty tissue at each pixel location. The inset photograph shows the sample as seen in the visible.

events. Lower noise also correlates to the higher shunt resistance, indicated by the right x -intercepts in Figure 4a. The detectivity is higher at 0 V than at reverse bias, because in our devices with an applied bias, the device noise increases faster than the EQE.^[14,35] The detectivity at zero bias D^* reaches up to 1.2×10^{11} Jones or $\text{cm Hz}^{1/2} \text{ W}^{-1}$ at the peak $\lambda = 1100$ nm. At this peak D^* level, the P1 BHJs with CA are comparable to commercial Ge photodiodes.^[4]

2.3. Spectroscopic Imaging via an Organic SWIR Photodiode Array

SWIR imaging benefits from enhanced penetration depths^[1] and accuracy^[2,36] with regard to minimally invasive tissue analyses. For example, since blood and fat tissues have strong absorption features in the SWIR, ischemia^[37] (inadequate blood flow) or atherosclerosis^[38] (fatty deposits clogging arteries) can be readily diagnosed by SWIR spectroscopy. Figure 6a shows clear differences in transmittance between muscle and fat, especially at $\lambda = 1210$ nm. The ability to distinguish fat and muscle tissues may assist laparoscopic procedures to enhance contrast between crucial organs and surrounding tissues. As such, SWIR imaging is highly desirable, but current technologies are costly and not affordable for wide deployment. Here, we demonstrate the feasibility to easily incorporate the organic photodiodes into a low-cost, scalable active matrix array that enables spatial mapping and compositional analysis of biological tissue.

Figure 6b illustrates our measurement setup for spectral imaging. To enable spatial mapping, a 4×4 active matrix array is integrated where each pixel is comprised of an organic photodiode connected to a silicon switching diode which reduces signal cross talk between neighboring pixels. The circuit diagram and pixel characterization are shown in Figure S6 (Supporting Information). To enable compositional analysis, the incident light is tuned to a narrow spectral range (10 nm of full width at half maximum) by using bandpass filters. To differentiate fatty tissues from muscle, we acquire measurements with two wavelengths, centered at $\lambda = 1152$ or 1200 nm. Fatty tissues display much stronger absorption at $\lambda = 1200$ nm compared to lean muscle. Meanwhile, both types of tissues show similar absorption at $\lambda = 1152$ nm, and thus signals will be normalized to this baseline at $\lambda = 1152$ nm, by calculating the transmittance

ratio $TR = \%T_{1200 \text{ nm}} / \%T_{1152 \text{ nm}}$. This normalization also adjusts for the background due to water, because the transmittance of water is nearly constant in the λ range of 1150 – 1250 nm (Figure S7, Supporting Information).

For the sample in Figure 6c inset, we stack three ≈ 1 mm thick beef slices together, to image the fat distribution under a lean muscle layer. Faint outlines of the region with high fat content on the top quarter section are observable in the visible spectrum; the fat buried in the bottom quarter region is harder to see in the visible but can be distinguished by the SWIR TR values in Figure 6c. We convert the TR values to estimate the fat percentage at each pixel location by $\text{fat}\% = (TR_{\text{sample}} - TR_{\text{muscle}}) / (TR_{\text{fat}} - TR_{\text{muscle}})$, where the values of TR_{muscle} and TR_{fat} are measured with 3 mm thick calibration standards that are visibly only lean muscle or only fat, respectively. The measurement uncertainty is $\approx 30\%$ due to light scattering artifacts and variations in calibration tissues. Nonetheless, the organic array is capable of providing contrast between fat and muscle tissues and shows promise for biomedical spectral imaging applications.

3. Conclusions

This study pinpoints the key mechanisms essential to raise EQE and detectivity in organic SWIR photodiodes. The CA additive increases dielectric permittivity without affecting the morphologies of two BHJ variants, and its role in the exciton dissociation and charge collection processes is revealed through measurements of film structures, transient photoconductivity, and electrochemical impedance. Dielectric screening reduces the exciton binding energy to increase exciton dissociation efficiency. The CA additive also redistributes the density of trap states and extends carrier lifetime, to lower trap-assisted recombination loss and improve charge transport and collection. The high-permittivity additive is general and particularly effective for SWIR BHJs, as the device performance is significantly improved and achieves a peak IQE of 66%, $\text{EQE} \approx 30\%$, and $D^* \approx 10^{11}$ Jones at $\lambda = 1100$ nm in the P1 BHJ with CA. The SWIR photodiodes are integrated into an active matrix to demonstrate tissue differentiation of muscle and fat by spectroscopic analysis, and this feasibility study presents a promising path to economical, scalable, high-performance organic detectors for the SWIR spectral region.

4. Experimental Section

Materials and Device Fabrication: The synthesis and characterization of P1 and P2 are described in the Supporting Information. Other chemicals were used as purchased. Glass substrates with indium tin oxide (resistivity $\approx 15 \Omega \text{ sq}^{-1}$) were sequentially cleaned by ultrasonication in detergent, deionized water, and isopropanol for 15 min. Poly(3,4-ethylenedioxythiophene) polystyrene sulfonate (Heraeus 4083) was mixed with isopropanol in 1:4 volume ratio. The solution was spin-cast onto the clean substrates and annealed at 130 °C for 10 min, to form 30 nm films that serve as an interfacial layer for hole extraction. The donor P1 or P2, acceptor PC₇₁BM, and CA additive were dissolved in dichlorobenzene with 3% 1,8-diiodooctane, and the blend solutions were spin-cast to form BHJ films with thicknesses ≈ 110 –175 nm, as measured by a stylus profilometer (Dektak). A ZnO nanoparticle solution was cast to form an ≈ 10 nm film for electron extraction. Then 100 nm Al was deposited through thermal evaporation to complete the photodiode structure. The devices were encapsulated with cover glass slides and glued onto the substrates with epoxy to allow characterization in ambient conditions.

Device Characterization: In the EQE measurements, the monochromatic light source was modulated at 400 Hz by an optical chopper, and the device photocurrent was amplified through a low-noise amplifier and measured with a lock-in amplifier (SRS 510). Optical filters with a cutoff wavelength at 455, 645, or 1025 nm were used to reduce the scattered light from higher order diffraction. The EQE is calculated with the expression $\text{EQE} = R(hc/\lambda q) = (J_{\text{ph}}/P_{\text{illum}})(hc/\lambda q)$, where h is Planck's constant, c is the speed of light, λ is the wavelength of the incident light, q is the electron charge, J_{ph} is the photocurrent density, P_{illum} is the intensity of the incident light, and R is the responsivity. The noise spectral densities were obtained by measuring the device through a preamplifier (SRS 570) connected to a power spectrum analyzer (HP 89410A).

The GIXD of polymeric thin films on silicon substrate was performed on a laboratory beamline system (Xenocs Inc., Xeuss 2.0) with an X-ray wavelength of 1.54 Å and sample-to-detector distance of 17.1 cm. An incidence angle of 0.2° was used. Samples were kept under vacuum to minimize air scattering. Diffraction images were recorded on a Pilatus 1M detector (Dectris Inc.) with an exposure time of 1 h and processed using the Nika software package, in combination with WAXSTools.

The R-SoXS measurements were performed in transmission mode in beamline 11.0.1.2 at Advanced Light Source. The film was floated in deionized water and transferred onto a 1.5 mm \times 1.5 mm silicon nitride window, then dried in air before being transferred into the vacuum chamber for R-SoXS. The photon energy was calibrated by measuring absorption spectra at the beamline and by comparison with near-edge absorption features of known spectra. Scattering was performed at 284.2 eV for P1, 284.0 eV for P2. These photon energies provide maximum scattering intensity for the particular samples. The scattered intensity was recorded by a back illuminated Princeton PI-MTE CCD thermoelectrically cooled to -45 °C. A modified version of the NIKA software package was used to process the scattering data. The samples were measured at two sample-to-detector distances, 50 and 150 mm separately for 10 s. These two regions were then stitched together to form the I - q line profile plots.

For transient photoconductivity measurements, a 520 nm pulsed laser with <10 ns pulse width was used as the light source. The intensity of the pulsed laser was $<20 \text{ mW cm}^{-2}$ to avoid space-charge effects. A 1.5 V battery connected in series to a potentiometer was used to apply a variable external bias on the photodiode. The photodiode was in series with the load resistor of 50 Ω , and the photocurrent was converted from the voltage drop across the load resistor. Each curve in Figure 3 is an average of 64 measurements as recorded by an oscilloscope, and it is also averaged over five trials for each applied bias.

Electrochemical impedance spectroscopy was performed with a Bio-Logic SP200 potentiostat in the dark and in the frequency range 3 Hz to 3 MHz. A small ac voltage of 20 mV was used, and this amplitude was low enough to maintain linearity of the response and high enough

to minimize measurement noise. The dc bias was at 0 V, except for the capacitance–voltage sweep from -3 to 0.5 V, in which the ac excitation was set at 5 kHz.

The transient photoconductivity measurements and electrochemical impedance spectroscopy are applicable to probe transport–recombination dynamics at a time scale of 0.1 μs or longer.

Pixel Array Integration and Spectroscopic Measurements: The photodiodes comprised of P1 BHJ with CA were integrated with silicon rectifiers (1N4007 Chanzon) as back-to-back diodes. For each pixel the photodiode area is 9 mm², and the silicon rectifiers were soldered onto a prototype board and then connected to photodiode electrodes by conductive epoxy (CW2460 Circuit Works). The active matrix's column and row traces were addressed with multiplexer chips (CD4053BE Texas Instruments) that interface with the voltage source and current readout pico-ammeter (Keithley 6487). During the reading of each pixel, the voltage source supplies 1.2 V, in which depending on the photocurrent ≈ 0.3 V forward bias was applied on the silicon rectifier to turn on the diode switch and the remaining ≈ 0.9 V was applied on the photodiode to reverse bias the device. The time interval used to read each pixel is 100 ms. The light intensity used in the measurement of Figure 6c is 0.3 mW cm⁻² at 1152 nm and 0.81 mW cm⁻² at 1200 nm. The transmittance percentage %T of a sample is calculated by the relation $\%T = (I_{\text{sample}} - I_{\text{dark}})/(I_{\text{blank}} - I_{\text{dark}})$, where I_{dark} is the dark current of the pixel, I_{sample} is the photocurrent measured when there is a sample between the light source and the photosensing pixel, and I_{blank} is the photocurrent with no sample.

Supporting Information

Supporting Information is available from the Wiley Online Library or from the author.

Acknowledgements

Z.W., Y.Z., W.Y., and T.N.N. are grateful for the support from American Chemical Society Petroleum Research Funds 57204-ND7 and from National Science Foundation (NSF ECCS-1839361). N.E., L.H., and J.D.A. are grateful for support from the Air Force Office of Scientific Research (AFOSR) through the Organic Materials Chemistry Program (Grant No. FA9550-17-1-0261) and the Army Research Labs (Grant No. W911NF-16-2-0189). S.Z. and X.G. thank USM for the start-up funding. This research used resources of the Advanced Light Source, which is a DOE Office of Science User Facility under Contract No. DE-AC02-05CH11231. Z.W. and T.N.N. designed the experiments and analyzed the data. Z.W., Y.Z., and W.Y. performed the device fabrication and characterization under T.N.N.'s direction. N.E. and L.H. carried out materials synthesis under J.D.A.'s direction. S.Z. took the X-ray diffraction measurements under X.G.'s direction. All authors discussed the results and contributed to the final manuscript.

Conflict of Interest

The authors declare no conflict of interest.

Keywords

dielectric screening, organic shortwave infrared photodiodes, spectroscopic imaging

Received: August 16, 2018
Revised: September 15, 2018
Published online:

- [1] O. T. Bruns, T. S. Bischof, D. K. Harris, D. Franke, Y. Shi, L. Riedemann, A. Bartelt, F. B. Jaworski, J. A. Carr, C. J. Rowlands, M. W. B. Wilson, O. Chen, H. Wei, G. W. Hwang, D. M. Montana, I. Coropceanu, O. B. Achorn, J. Kloepper, J. Heeren, P. T. C. So, D. Fukumura, K. F. Jensen, R. K. Jain, M. G. Bawendi, *Nat. Biomed. Eng.* **2017**, 1, 0056.
- [2] R. H. Wilson, K. P. Nadeau, F. B. Jaworski, B. J. Tromberg, A. J. Durkin, *J. Biomed. Opt.* **2015**, 20, 030901.
- [3] A. Rogalski, *Infrared Phys. Technol.* **2011**, 54, 136.
- [4] F. P. García De Arquer, A. Armin, P. Meredith, E. H. Sargent, *Nat. Rev. Mater.* **2017**, 2, 16100.
- [5] K. J. Baeg, M. Binda, D. Natali, M. Caironi, Y. Y. Noh, *Adv. Mater.* **2013**, 25, 4267.
- [6] R. D. Jansen-van Vuuren, A. Armin, A. K. Pandey, P. L. Burn, P. Meredith, *Adv. Mater.* **2016**, 28, 4766.
- [7] T. N. Ng, W. S. Wong, M. L. Chabinyc, S. Sambandan, R. A. Street, *Appl. Phys. Lett.* **2008**, 92, 213303.
- [8] X. Gong, M. Tong, Y. Xia, W. Cai, J. S. Moon, Y. Cao, G. Yu, C.-L. Shieh, B. Nilsson, A. J. Heeger, *Science* **2009**, 325, 1665.
- [9] L. Dou, Y. Liu, Z. Hong, G. Li, Y. Yang, *Chem. Rev.* **2015**, 115, 12633.
- [10] J. Han, D. Yang, D. Ma, W. Qiao, Z. Y. Wang, *Adv. Opt. Mater.* **2018**, 1800038.
- [11] A. London, L. Huang, B. Zhang, B. Oviedo, J. Tropp, W. Yao, Z. Wu, B. Wong, T. N. Ng, J. D. Azoulay, *Polym. Chem.* **2017**, 8, 2922.
- [12] L. Zheng, T. Zhu, W. Xu, L. Liu, J. Zheng, X. Gong, F. Wudl, *J. Mater. Chem. A* **2018**, 6, 3634.
- [13] K. H. Hendriks, W. Li, M. M. Wienk, R. A. J. Janssen, *J. Am. Chem. Soc.* **2014**, 136, 12130.
- [14] Z. Wu, W. Yao, A. E. London, J. D. Azoulay, T. N. Ng, *Adv. Funct. Mater.* **2018**, 28, 1800391.
- [15] J. Benduhn, K. Tvingstedt, F. Piersimoni, S. Ullbrich, Y. Fan, M. Tropicano, K. A. McGarry, O. Zeika, M. K. Riede, C. J. Douglas, S. Barlow, S. R. Marder, D. Neher, D. Spoltore, K. Vandewal, *Nat. Energy* **2017**, 2, 17053.
- [16] R. A. Street, A. Krakaris, S. R. Cowan, *Adv. Funct. Mater.* **2012**, 22, 4608.
- [17] L. J. A. Koster, S. E. Shaheen, J. C. Hummelen, *Adv. Energy Mater.* **2012**, 2, 1246.
- [18] X. Liu, B. Xie, C. Duan, Z. Wang, B. Fan, K. Zhang, B. Lin, F. J. M. Colberts, W. Ma, R. A. J. Janssen, F. Huang, Y. Cao, *J. Mater. Chem. A* **2018**, 6, 395.
- [19] I. Constantinou, X. Yi, N. T. Shewmon, E. D. Klump, C. Peng, S. Garakyaraghi, C. K. Lo, J. R. Reynolds, F. N. Castellano, F. So, *Adv. Energy Mater.* **2017**, 7, 1601947.
- [20] K. S. Nalwa, J. A. Carr, R. C. Mahadevapuram, H. K. Kodali, S. Bose, Y. Chen, J. W. Petrich, B. Ganapathysubramanian, S. Chaudhary, *Energy Environ. Sci.* **2012**, 5, 7042.
- [21] S. Leblebici, J. Lee, A. Weber-Bargioni, B. Ma, *J. Phys. Chem. C* **2017**, 121, 3279.
- [22] B. Bernardo, D. Cheyns, B. Verreert, R. D. Schaller, B. P. Rand, N. C. Giebink, *Nat. Commun.* **2014**, 5, 3245.
- [23] S. O. Morgan, W. A. Yager, *Ind. Eng. Chem.* **1940**, 32, 1519.
- [24] R. A. Street, S. Cowan, A. J. Heeger, *Phys. Rev. B: Condens. Matter Mater. Phys.* **2010**, 82, 11.
- [25] R. C. I. Mackenzie, C. G. Shuttle, G. F. Dibb, N. Treat, E. Von Hau, M. J. Robb, C. J. Hawker, M. L. Chabinyc, J. Nelson, *J. Phys. Chem. C* **2013**, 117, 12407.
- [26] R. A. Street, *Phys. Rev. B* **2011**, 84, 075208.
- [27] F. Fabregat-Santiago, G. Garcia-Belmonte, I. Mora-Seró, J. Bisquert, *Phys. Chem. Chem. Phys.* **2011**, 13, 9083.
- [28] R. A. Street, Y. Yang, B. C. Thompson, I. McCulloch, *J. Phys. Chem. C* **2016**, 120, 22169.
- [29] T. Walter, R. Herberholz, C. Müller, H. W. Schock, *J. Appl. Phys.* **1996**, 80, 4411.
- [30] V. D. Mihailetchi, L. J. A. Koster, J. C. Hummelen, P. W. M. Blom, *Phys. Rev. Lett.* **2004**, 93, 19.
- [31] N. A. Ran, S. Roland, J. A. Love, V. Savikhin, C. J. Takacs, Y. T. Fu, H. Li, V. Coropceanu, X. Liu, J. L. Brédas, G. C. Bazan, M. F. Toney, D. Neher, T. Q. Nguyen, *Nat. Commun.* **2017**, 8, 79.
- [32] K. Vandewal, S. Albrecht, E. T. Hoke, K. R. Graham, J. Widmer, J. D. Douglas, M. Schubert, W. R. Mateker, J. T. Bloking, G. F. Burkhard, A. Sellinger, J. M. J. Fréchet, A. Amassian, M. K. Riede, M. D. McGehee, D. Neher, A. Salleo, *Nat. Mater.* **2014**, 13, 63.
- [33] S. Torabi, F. Jahani, I. Van Severen, C. Kanimozhi, S. Patil, R. W. A. Havenith, R. C. Chiechi, L. Lutsen, D. J. M. Vanderzande, T. J. Cleij, J. C. Hummelen, L. J. A. Koster, *Adv. Funct. Mater.* **2015**, 25, 150.
- [34] I. R. Gould, S. Farid, *J. Phys. Chem. B* **2007**, 111, 6782.
- [35] Z. Wu, W. Yao, A. E. London, J. D. Azoulay, T. N. Ng, *ACS Appl. Mater. Interfaces* **2017**, 9, 1654.
- [36] R. Nachabé, B. H. W. Hendriks, M. van der Voort, A. E. Desjardins, H. J. C. M. Sterenborg, *Biomed. Opt. Express* **2010**, 1, 1432.
- [37] H. Akbari, Y. Kosugi, K. Kojima, N. Tanaka, *IEEE Trans. Biomed. Eng.* **2010**, 57, 2011.
- [38] S. Shang, Z. Chen, Y. Zhao, S. Yang, D. Xing, *Opt. Express* **2017**, 25, 530.